NeuroImage 187 (2019) 93–103

Contents lists available at ScienceDirect

NeuroImage

journal homepage: www.elsevier.com/locate/neuroimage

A stereotaxic breed-averaged, symmetric T2w canine brain atlas including detailed morphological and volumetrical data sets

Björn Nitzsche [a,b,*], Johannes Boltze [c], Eberhard Ludewig [d], Thomas Flegel [e], Martin J. Schmidt [f], Johannes Seeger [b], Henryk Barthel [a], Olivia W. Brooks [g], Matthew J. Gounis [g], Michael H. Stoffel [h,1], Sabine Schulze [f,1]

[a] Department for Nuclear Medicine, University Hospital of Leipzig, Leipzig, Germany
[b] Institute of Anatomy, Histology and Embryology, Faculty of Veterinary Medicine, University of Leipzig, Leipzig, Germany
[c] Department of Translational Medicine and Cell Technology, Fraunhofer Research Institution for Marine Biotechnology and Cell Technology, Institute of Medical and Marine Biotechnology, University of Lübeck, Lübeck, Germany
[d] Clinic Unit of Diagnostic Imaging, University of Veterinary Medicine Vienna, Austria
[e] Department of Small Animals Medicine, Veterinary Faculty, University of Leipzig, Leipzig, Germany
[f] Department of Veterinary Clinical Sciences, Clinic for Small Animals - Neurosurgery, Neuroradiology and Clinical Neurology, Faculty of Veterinary Medicine, Justus-Liebig-University Gießen, Gießen, Germany
[g] Department of Radiology, New England Center for Stroke Research, University of Massachusetts Medical School, Worcester, MA, USA
[h] Division of Veterinary Anatomy, Vetsuisse Faculty, University of Bern, Bern, Switzerland

ARTICLE INFO

Keywords:
Brain
Atlas
Tissue segmentation
MRI
Dog
Canine
Stereotaxy

ABSTRACT

Stereotaxic systems and automatic tissue segmentation routines enable neuronavigation as well as reproducible processing of neuroimage datasets. Such systems have been developed for humans, non-human-primates, sheep, and rodents, but not for dogs. Although dogs share important neurofunctional and -anatomical features with humans, and in spite of their importance in translational neuroscience, little is known about the variability of the canine brain morphology and, possibly related, function. Moreover, we lack templates, tissue probability maps (TPM), and stereotaxic brain labels for implementation in standard software utilities such as Statistical Parametric Mapping (SPM). Hence, objective and reproducible, image-based investigations are currently impeded in dogs. We have created a detailed stereotaxic reference frame for dogs including TPM and tissue labels, enabling inter-individual and cross-study neuroimage analysis.

T2w datasets were acquired from 16 neurologically inconspicuous dogs of different breeds by 3T MRI. The datasets were averaged after initial preprocessing using linear and nonlinear registration algorithms as implemented in SPM8. TPM for gray (GM) and white matter (WM) as well as cerebrospinal fluid (CSF) were created. Different cortical, subcortical, medullary, and CSF regions were manually labeled to create a spatial binary atlas being aligned with the template. A proof-of-concept for automatic determination of morphological and volumetrical characteristics was performed using additional canine datasets (n = 64) including a subgroup of laboratory beagles (n = 24).

Overall, 21 brain regions were labeled using the segmented tissue classes of the brain template. The proof-of-concept trial revealed excellent suitability of the created tools for image processing and subsequent analysis. There was high intra-breed variability in frontal lobe and hippocampus volumes, and noticeable inter-breed corpus callosum volume variation.

The T2w brain template provides important, breed-averaged canine brain anatomy features in a spatial standard coordinate system. TPM allows automatic tissue segmentation using SPM and enables unbiased automatic image processing or morphological characterization in different canine breeds. The reported volumetric and morphometric results may serve as a starting point for further research aimed at *in vivo* analysis of canine brain anatomy and function.

* Corresponding author. Department for Nuclear Medicine, University Hospital of Leipzig, Leipzig, Germany, Liebigstraße 18, 04103 Leipzig, Germany.
E-mail address: bjoern.nitzsche@medizin.uni-leipzig.de (B. Nitzsche).
[1] Contribute equally to this work.

https://doi.org/10.1016/j.neuroimage.2018.01.066
Received 29 September 2017; Received in revised form 17 January 2018; Accepted 25 January 2018
Available online 31 January 2018

Introduction

Neuroimaging provides key information on brain morphology and function. Cutting-edge image processing routines require spatial standards such as stereotaxic references when assigning for spatial comparability of classified tissue compartments (Ashburner and Friston, 2000, 2005). Thus, stereotaxic templates and *a priori tissue* classification were established for several species including humans (Xiao et al., 2017), non-human primates (Frey et al., 2011), sheep (Nitzsche et al., 2015), rats (Papp et al., 2014) and mice (Bai et al., 2012). All use conventions as defined by the Montreal Neurological Institute (MNI). However, similar data are still lacking for the dog, not reflecting the relevance of this species in veterinary medicine and translational neuroscience research.

Canine cranium anatomy displays enormous diversity as a result of selective breeding endeavors over the past 30.000 years. Available population-averaged canine brain templates disregard these features (Datta et al., 2012), relying on a limited number of breeds only (Su et al., 2005), or are based on non-cerebral anatomical surrogates such as skull bone classification although a correlation with cerebral morphology has not been shown (Milne et al., 2016). Moreover, none of these approaches considers the potential cerebral cross-breed variability.

Consequently, a comparative cross-breed morphological characterization of the canine brain in clinical or experimental individuals and cohorts is still lacking and spatial features of the canine brain have not yet been described in much detail. Such evidence has potential to greatly enhance research on canine geriatric abnormalities (Noh et al., 2017), anatomical malformations (Bernardino et al., 2015), and localization of brain functions (Dilks et al., 2015).

We herein present a canine neuroimage reference dataset which considers the inter-breed variability. The data set includes a stereotaxic, breed-averaged, symmetric T2w template, tissue probability maps (TPM) for gray (GM) and white matter (WM) as well as cerebrospinal fluid (CSF) classification, and a spatially aligned labeled brain atlas. Using Statistical Parametric Mapping (SPM, Wellcome Trust Center for Neuroimaging), we further assessed data set applicability (i) on a clinical cohort comprised of different breeds and (ii) on a homogeneous cohort of laboratory beagles.

Materials and methods

Cranial image data from different canine breeds were obtained from two institutions: One data set was provided by the Department of Small Animal Medicine, Veterinary Faculty, University Leipzig (*Leipzig* dataset). Data was recorded between 2014 and 2015 during clinical routine. The second data set (acquired in 2013) was obtained from laboratory beagles being investigated at the Department of Radiology, New England Center for Stroke Research, University of Massachusetts Medical School, Worcester, Massachusetts, USA (*Worcester* dataset).

Study population

Any data set from subjects with inherent structural brain alterations and/or neurological deficits was excluded. All datasets were randomized and anonymized prior to image processing.

The Leipzig dataset comprised 36 T2w MRI investigations. Animal age ranged from 1 to 16 years. 20 different breeds were included (male/female/average body weight in kilogram): Labrador Retriever (3/4/34.4); Miniature Schnauzer (1/0/8.7); Pomeranian (0/1/2.1); Hovawart (2/0/40.0); Hanoverian Scenthound (0/1/40.0); Border Collie (0/1/33.0); Shetland Sheepdog (1/1/7.5); Jack-Russel Terrier (0/1/12.0); Dalmatian (1/0/23.0); Boxer (0/1/26.0); French Bulldog (2/0/16.0); Dogue de Bordeaux (0/1/40.0); Airedaile Terrier (1/0/36.0); Bernese Mountain Dog (0/1/48.5); Beagle (1/0/20.5); Rhodesian Ridgeback (2/0/49.5); Australian Shepherd (1/1/23.5); Papillon (0/1/2.2); Yorkshire Terrier (1/0/3.2); mixed breeds (6/0/19.2). No animal protocol was required since animals were imaged in clinical routine only.

The Worcester dataset comprised 24 laboratory beagles (female/body weight 10.8, 95% CI:10.3–11.2 kg, Marshall BioResources, New York, United States) and thus provided a homogeneous study population. Age ranged from 1 to 7 years. MRI was performed prior to any experimental purposes: The subjects were enrolled to baseline imaging, so none interfered with this study. Animal research activities were approved by the local Institutional Animal Care and Use Committee (Animal Welfare Assurance No.: D16-00196 (A3306-01)).

Image acquisition

MR imaging (Leipzig dataset) was performed using transverse (Leipzig 1) and sagittal (Leipzig 2) T2w Turbo Spin Echo (TSE) sequence on a 3T System (Ingenia, Philips Healthcare, Healthcare, Eindhoven, The Nederlands; for details please see Table 1). The Worcester dataset includes transverse T2w Fast Field Echography (FFE) MRI sequences, which were obtained using a 3T system (Achieva, Philips Healthcare, Healthcare, Eindhoven, The Nederlands; for details please see Table 1). All animals were placed in prone position and received volatile anesthesia (2% isoflurane) with mechanical respiration during MR imaging.

T2w TSE template and tissue probability map (TPM)

Sixteen T2w MRI datasets with transverse and sagittal scans from each subject were randomly chosen from the Leipzig database to generate the stereotaxic, breed averaged MR template and corresponding tissue probability maps (TPM). Image processing was performed using SPM8 (http://www.fil.ion.ucl.ac.uk/spm/software/spm8/) (Ashburner & Friston, 2011), implemented in Matlab 2015a (The Mathworks Inc., USA) and 'Fiji is just ImageJ' (Fiji) (Schindelin et al., 2012). Manual delineation, revision of tissue masks by excluding misclassified voxel and final evaluation were iteratively performed by three experienced investigators (veterinary radiologists/anatomists). All individual datasets were converted to the NIFTI-1 format using the software dcm2nii (Li et al., 2016) prior to further processing. The workflow chart for the following steps is given in Fig. 1. Step 1 initiated the procedure by (i) preparing high-quality structure-preserving input images averaging the transversal (Leipzig1) and sagittal (Leipzig2) T2w TSE sequences in MNI coordinate system (AVG0, group average = $AVG0^{mean}$). Rigid coregistration resulted in aligned individual images (AVG1, group average = $AVG1^{mean}$). Step 2 included the preparation of the rigidly coregistered GM/WM/CSF tissue masks for each individual including correction for intensity inhomogeneity and lateralization. In Step 3 affine coregistration (AVG2, group average = $AVG2^{mean}$) and nonlinear alignment of each individual (AVG3, group average = $AVG3^{mean}$) was performed. In detail:

Step I. The corresponding transverse and coronal T2w TSE images were reoriented according to the MNI definition using SPM8. The anterior commissure (AC; named rostral commissure in quadrupeds (Constantinescu et al., 2012)) served as the point-of-origin of the Cartesian coordinate system. The y-axis passed the posterior commissure (PC; named caudal commissure in quadrupeds (Constantinescu et al., 2012)).

Table 1
Description of MRI sequences.

Parameter	Location		
	Leipzig 1	Leipzig 2	Worcester
Sequence	T2w TSE	T2w TSE	T2w FFE
Scan direction	transverse	sagittal	transverse
Voxel size (scan direction)	0.23 × 0.23 × 2.2	0.38 × 0.38 × 6.0	0.5 × 0.5 × 2.0
Acquisition matrix	452 × 340	204 × 152	128 × 128
TE/TR	100/4552	4.6/11	16.1/1200
Flip angle	90	15	18
Others	SENSE	SENSE	SENSE

X-axis values increase from left to right and z-axis values increase in dorsal direction. Subsequently, all MR data were resliced to an isotropic voxel size of 0.5 mm edge length, followed by individual coregistration with transversal images serving as references. Individual transversal and sagittal data were corrected for Gaussian/Rician noise using non-local mean filter SANLM (Manjon et al., 2010) and intensity inhomogeneity (Sled et al., 1998). Transverse and sagittal MR scans belonging together were then averaged (Avg0) and the population mean ($Avg0^{mean}$) was calculated. Then, all Avg0 were rigidly coregistered (6 degrees of freedom using 6th order B-spline interpolation) to $Avg0^{mean}$ in order to create Avg1. These were subsequently averaged ($Avg1^{mean}$).

Step II. Initially, GM, WM and CSF masks of 4 randomly chosen Avg1 were created using a combination of intensity-based segmentation and manual delineation in Fiji. The tissue classes were averaged and the resulting images were smoothed with a Gaussian kernel (full width half maximum, FWHM) of 2 mm. The smoothed GM, WM and CSF served as initial TPM, and were implemented in SPM8 for subsequent automatic segmentation procedure of the initial four Avg1. A relatively large Gaussian kernel of 3 mm was chosen for each tissue class to automatically recover the GM, WM, and CSF masks. Any misclassified voxels in each tissue class were manually removed using Fiji. The procedure was repeated 3 times adding 4 more Avg1 at every iteration before the resulting 16 final Avg1 were segmented and refined. Finally, copies of all tissue classes and corresponding Avg1 were flipped along the x-axis resulting in a dataset of 32 subjects.

Step III. Since dogs exhibit extensive amount of extracranial soft tissue, the brain tissue mask was normalized by calculating the sum of the GM and WM mask (affine transformation with 12 degree of freedom using 6th order B-spline interpolation) with $Avg1^{mean}$ serving as stationary reference. Refined brain tissue masks (GM, WM) of Step II without skull and eye tissue were used (see Fig. 1) for the higher dimensional wrapping procedures 'Normalization' (= affine coregistration) and DARTEL. Avg2

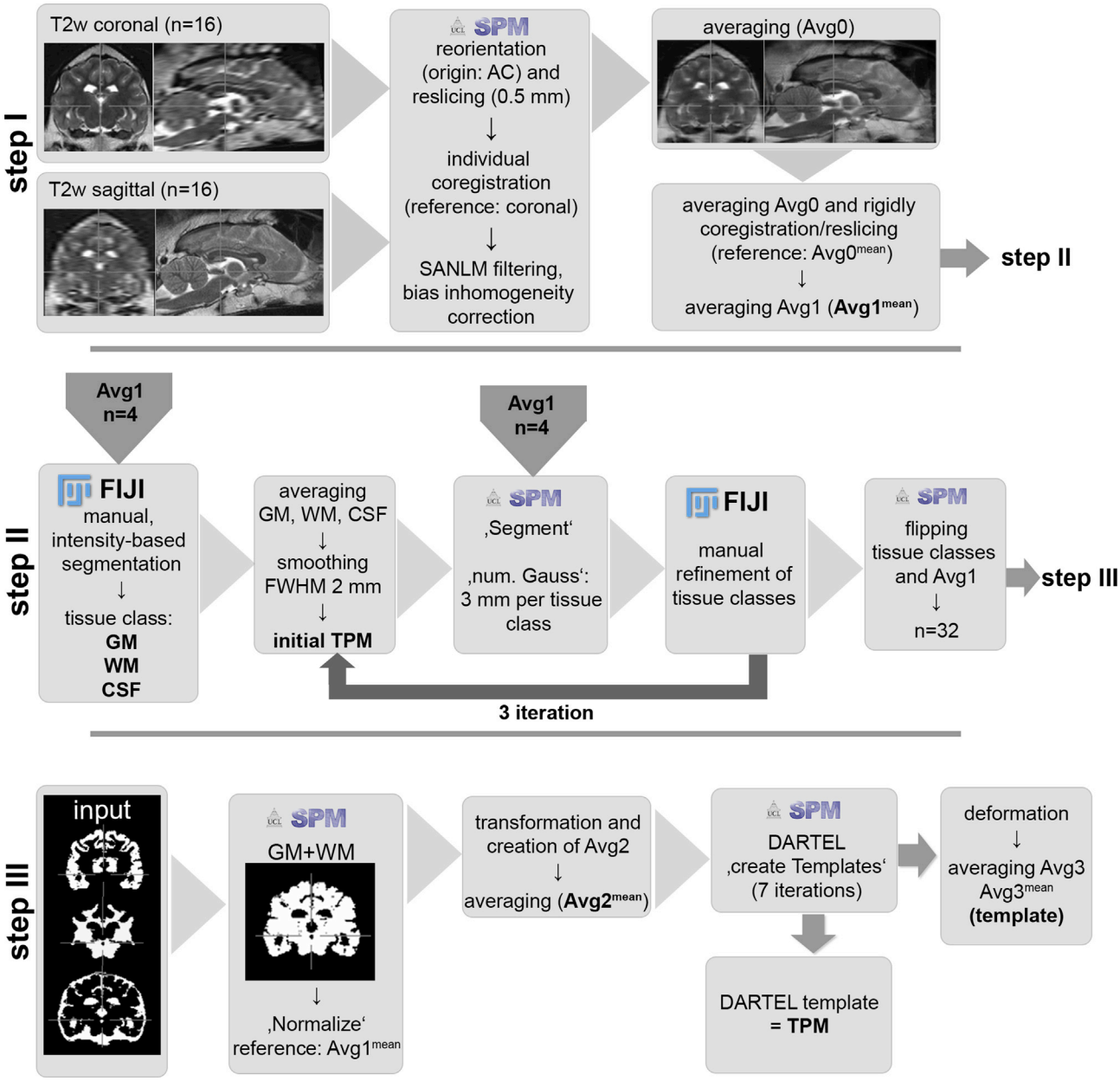

Fig. 1. Image processing workflow. Schematic illustrations of working steps applied for generation of the canine breed-averaged, symmetric, unbiased T2w template and tissue probability maps (TPM). AC – Anterior Commissure; SANLM – Spatial Adaptive Non-Local Mean filter; Avg – averaged image; GM – Gray matter; WM – White matter; CSF – Cerebrospinal fluid; FWHM – Full Width Half Maximum; TPM – Tissue probability maps.

were created by applying the retrieved transformation matrices to corresponding tissue classes of Avg1. This was followed by averaging to create the Avg2^{mean}. Subsequently, the normalized GM, WM, and CSF masks served as input for the coregistration of the individual properties in one space with 'Diffeomorphic Registration Algorithm' (DARTEL) (Ashburner, 2007) by using standard justification except for increasing the number of iterations by one, and decreasing the smoothing parameter stepwise: [16 8 4 2 1 0.5 0.5]. The resulting deformation maps were applied to Avg2 (creating Avg3), followed by averaging them to form the final breed-averaged, symmetric T2w TSE template (Avg3^{mean}). The averaged and highly coregistered tissue classes of the 6th iteration served as final TPMs.

Morphological characteristics and tissue preparation

The brain of a Labrador retriever (euthanasia due to congestive heart failure) was retrieved for routine autopsy at the Institute for Veterinary Pathology, Faculty of Veterinary Medicine, University of Leipzig, Germany. The brain was immersion-fixed in *in toto* with 4% buffered paraformaldehyde (pH = 7.4) to compare topological and anatomical features with template properties. After 8 weeks, the brain was photographed in all planes (DSLR Canon 600D) and cut into 4 mm equal spaced coronal slices. Photographs were taken from rostral and caudal planes of every slice.

GM and WM surface reconstruction from the tissue classes of the template (=Avg3^{mean}) was performed using the integrated 3D viewer plugin for Fiji (Version: 1.50e with Java 1.6.0_24). All data was stored as .obj files for further use. Additionally, 3D volume was constructed from the segmented template brain tissue for comparative topology using the integrated FIJI plugin VolumeViewer (Version 2.01).

Topological and anatomical labeling of structures identified in the brain specimen and the averaged T2w template was performed according to established standards in the neuroanatomical literature (Adrianov et al., 2010) and Nomina Anatomica Veterinaria 2012 (NAV 2012) with the exception of the rostral (anterior) and caudal (posterior) commissures (see above).

Quality inspection

Quality of the averages Avg1^{mean}, Avg2^{mean}, and Avg3^{mean} as well as of individual original image volumes was assessed by calculating signal-to-noise (SNR) and contrast-to-noise (CNR) ratios according to equations (1) and (2):

$$SNR = \frac{mean^{gV}\ per\ ROI^{i}}{sd\ per\ ROI^{i}} \tag{1}$$

$$CNR = \frac{mean^{gV}_{ROI^{i}} - mean^{gV}_{WM}}{\sqrt[2]{var_{ROI^{i}} + var_{WM}}} \tag{2}$$

where *gV* is the gray value, *sd* the standard deviation and *var* the variance. Herein, caudate nucleus (Ncc), temporal lobe and the WM served as regions of interest (ROI^{i}; with Ncc: i = 1, temporal lobe: i = 2 and WM: i = 3). CNR ratios were calculated between Ncc and WM as well as between temporal lobe and WM. The SNR ratio represents the homogeneity of gray values within a tissue class while the CNR ratio describes the mean gray value difference between WM and GM.

Further, DICE (3) and Jaccard (4) similarity coefficients were calculated to analyze the incidence of concordance between manual and automatic segmentation for (i) 'Unified Segmentation' procedure in SPM8 (Ashburner and Friston, 2005) and (ii) atlas based segmentation according to the equations (3) and (4):

$$DICE = \frac{2|A \cap B|}{|A| + |B|} \tag{3}$$

$$Jaccard = \frac{|A \cap B|}{|A \cup B|} \tag{4}$$

Coefficients of automatic (A) and manually (B) segmented tissue classes were compared to determine segmentation quality. The caudate nucleus was chosen to analyze the quality of atlas based segmentation procedure by inversely applying the atlas labels to individual space.

Additionally, the point-to-point distance of surface meshes (= Hausdorff distance) between the aforementioned automatically and manually segmented tissue classes for (i) and (ii) (Beauchemin et al., 1998) were calculated, compared and visualized using the Computational Anatomy Toolbox (Gaser and Dahnke, 2016) in SPM12.

Preparation of the spatial tissue labels

All structures of interest were delineated by using manual and intensity-based segmentation in at least two planes. The procedure included the synchronous visualization of GM, WM or CSF masks with the template using the FIJI plugin SyncWindow. Each structure was binary-labeled using a unique gray value. The final atlas included all given labels aligned with the template, and was stored as 8-bit-binary NIFTI-1 file.

Proof-of-concept: automatic segmentation in SPM8 and volumetry

The created template and TPMs were utilized to test the MR image preprocessing capability using SPM8. Transversal T2w TSE MRI scans of the Leipzig1 dataset were used. Data sets of 20 additional dogs from Leipzig1 dataset were added (in total 36 clinical cases). 24 MRI scans of laboratory beagles from the Worcester database were used as a phenotypically homogenous group.

All original images were reoriented according to the canine space (see above) and co-registered to the T2w TSE template using SPM8 with standard parameters except for a 6th-B-spine interpolation. GM, WM, and CSF masks were automatically created from all animals using the SPM8 segmentation routine with standard parameters except for "num. Gaussians", for which smaller values [1 1 2] and a slightly decreased sampling distance (1 mm) were chosen. Subsequently, all tissue masks were carefully inspected for segmentation errors. Remaining non-brain tissue voxels were manually removed in Fiji.

Brain tissue volumetry was performed using reverse high dimensional warping of the atlas labels into individual space as follows: GM and WM mask were nonlinearly coregistered to the former GM and WM DARTEL TPM of the 7th iteration. The resulting deformation fields were reversely applied to the atlas labels and transformed into individual spaces.

Finally, the absolute volumes for individual GM, WM, and CSF (in mL) as well as cortical, subcortical and cerebellar structures were determined using Matlab SPM8 script get_totals (Author: Ged Ridgway; http://www0.cs.ucl.ac.uk/staff/g.ridgway/vbm/get_totals.m). The total brain volume was calculated by the sum of GM and WM. Additionally, brain tissue indices, in particular the ratios between absolute GM and WM ($I^{GM:WM}$) volume as well as GM and total brain ($I^{GM:brain}$) volume were computed. The Quartile Coefficient of Dispersion (QCD) was calculated from every tissue volume and brain indices to enable comparison for relative variation in respect to median and quartile according to equation (5):

$$QCD = \frac{3rd\ quartile - 1st\ quartile}{median} \tag{5}$$

Statistics

ANOVA was performed to compare SNR and CNR ratios in original transversal MR data, Avg0, Avg1^{mean}, Avg2^{mean} and Avg3^{mean}. Group-wise comparison between brain volumes from Leipzig and Worcester datasets was performed considering absolute tissue volume, as well as

brain tissue indices ($I^{GM:WM}$ and $I^{GM:brain}$) using Matlab 2015a. P-values <0.05 were considered statistically significant. Descriptive statistics of all boxplots include 95% confidence intervals (CI, whisker), 1st and 3rd quantiles (box), medians (bar) and outliers exceeding the CI (+).

Results

The canine breed-averaged, symmetric T2w TSE template and stereotactic coordinate system

The DARTEL-transformed canine brain template ($Avg3^{mean}$) and corresponding TPM provided better resolution than individual samples (Fig. 2A). The canine coordinate system was implemented into a grid of 0.5 mm isotropic voxel size. The AC represents the coordinate origin, the y-axis passes the PC at coordinates [x; y;z] at [0;-16; 0]. Values of the x-axis increase from left to right and z-axis values from inferior to superior (Fig. 3).

The template represents the intensity and spatial positioning of the averaged anatomical brain structures. None of the samples included relevant mirroring, aliasing or motion artifacts. Bias inhomogeneity, magnetic susceptibility and Gibbs/truncation artifacts were marginal.

$Avg1^{mean}$ and $Avg2^{mean}$ were blurred and featured insufficient detail resolution. Compared to the individual T2w TSE samples, the $Avg3^{mean}$ (DARTEL template, Fig. 2A) showed a significantly better SNR ($p < 0.05$; Fig. 2B). The standard deviation of gray valued for each voxel inside the cranial cavity decreased after affine ($Avg1^{mean}$) and non-linear ($Avg2^{mean}$) registration (Fig. 2A). As expected, the SNR in $Avg1^{mean}$ and $Avg2^{mean}$ were significantly lower than in the $Avg3^{mean}$ ($p < 0.05$, Fig. 2B). The CNR increased significantly during postprocessing which contributed to the improved detail resolution of $Avg3^{mean}$ ($p < 0.05$). However, the CNR of earlier processing steps ($Avg1^{mean}$, $Avg2^{mean}$) showed less contrast compared to the CNR of individual MRI ($p < 0.05$, Fig. 2C).

Morphological characteristics

The canine breed-averaged template was comprised of T2w images from 16 subjects. Three-dimensional surface reconstruction of the segmented canine GM and WM from the cerebrum and cerebellum revealed a detailed morphological topography (Fig. 3).

In both the dissected brain and the rendered volume, primary, secondary and tertiary gyrus formations were clearly differentiable (Fig. 4). All major subcortical nuclei were clearly detectable in coronal brain sections and in the T2w template (Fig. 5A).

TPM and segmentation

TPM for the canine stereotaxic space was generated from 16 subjects. Tissue probabilities for GM, WM, and CSF included the cerebrum, cerebellum and medulla oblongata. The resolution of the TPM with an isotropic voxel size of 0.5 mm allowed a detailed, automated segmentation procedure. The segmented GM, WM and CSF masks of the template

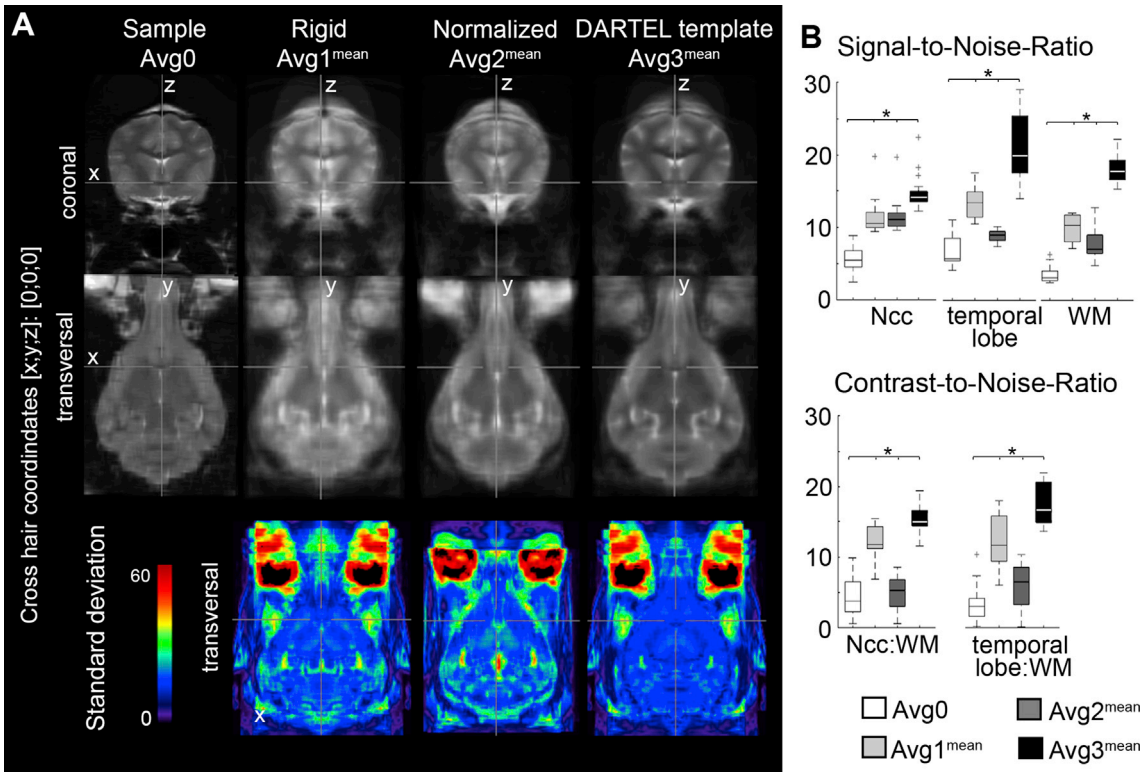

Fig. 2. Averages during processing. (A) Coronal and transverse planes of averages after initial averaging of two T2w MRI sequences in different planes (Avg0, sample), rigid coregistration ($Avg1^{mean}$), normalization ($Avg2^{mean}$), and the final DARTEL transformed template ($Avg3^{mean}$): All images have an isotropic voxel size of 0.5 mm and were registered according to the canine stereotactic coordinate system. This enables visual comparison during the template creation process. The high degree of alignment within the $Avg3^{mean}$ led to an improved boundary delineation and increased detail resolution. Coronal planes of the standard deviation from $Avg1^{mean}$, $Avg2^{mean}$ and $Avg3^{mean}$ show the standard deviation inside the cranial cavity which increased after affine and decreased after non-linear DARTEL registration. A RGB lookup table was applied for better visualization of voxel values. Stereotaxic coordinates are given in mm. (B) SNR and CNR: SNR of $Avg1^{mean}$, $Avg2^{mean}$ and the sample data (Avg0), were significantly increased compared to SNR of $Avg3^{mean}$ in ROIs for caudate nucleus (Ncc), temporal lobe and white matter (WM). Furthermore, the CNR significantly increased in $Avg3^{mean}$ after rigid and normalized transformation. The comparison between each Avg0 and $Avg3^{mean}$ revealed a significantly increased CNR in the DARTEL transformed, population-averaged brain template (*$p < 0.05$. "+" depict outliers). $Avg0/1^{mean}/2^{mean}/3^{mean}$ – Averages after initiation, rigid coregistration, normalization and DARTEL transformation, respectively; SNR - Signal-to-Noise-Ratio; CNR - Contrast-to-Noise-Ratio; *p-value < 0.05 (ANOVA).

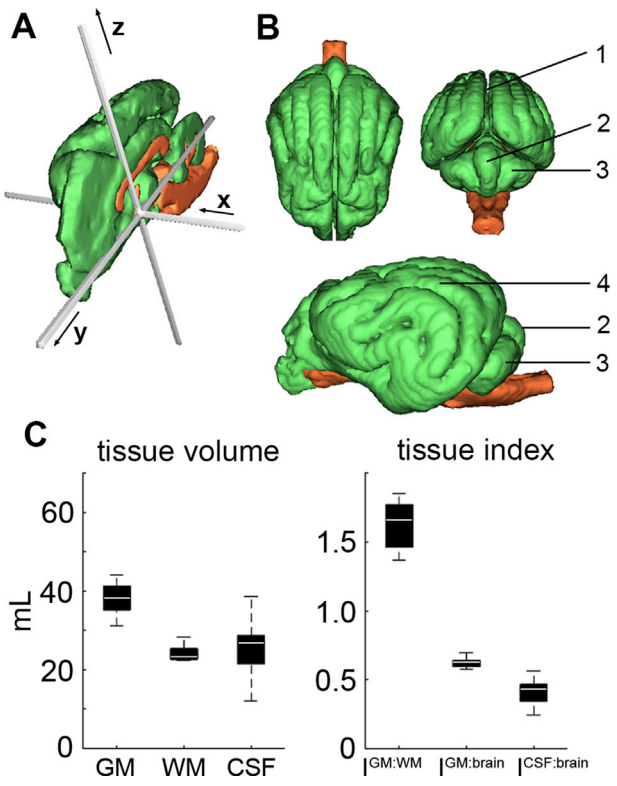

Fig. 3. Canine stereotaxic coordinate system. (A) Surface reconstruction from GM (green) and WM (orange) masks of the template. The stereotaxic coordinate system was applied according to the definition of the Montreal Neurological Institute (MNI). Arrows indicate the increase of x, y or z coordinates. (B) Dorsal, caudal and lateral view of the canine brain surface composed of GM (green) and WM (orange) surfaces. Sulci and gyri are clearly distinguishable. (C) Descriptive parameters of the templates tissue classes. 1 – Longitudinal fissure; 2 – Vermis; 3 – cerebellar hemisphere; 4 – Left cerebral hemisphere; GM - Gray matter; WM - White matter; CSF - Cerebrospinal fluid; $I^{GM:WM}$, $I^{GM:brain}$, $I^{CSF:brain}$ - brain index: ratio between GM and WM volume, GM and brain volume and between CSF and brain volume, respectively.

(Avg3^{mean}) did not contain any misclassified voxels (Fig. 3).

Spatial similarity between manual and automatic segmentation procedures for 'Unified segmentation' procedure in SPM8 were calculated as 0.67 ± 0.06 (DICE's correlation coefficient; 0.56/0.73, minimum/maximum) and 0.50 ± 0.07 (Jaccard's similarity coefficient, 0.39/0.57, minimum/maximum). The Hausdorff distance between manual and automatically segmented surface meshes was 5.58 ± 1.04 (mean distance error: 0.77 ± 0.11 mm) (supplementary Figure A1 for representative individuals).

The spatial similarity between manually and automatically segmented caudate nucleus using the atlas approach revealed DICE's coefficient of 0.71 ± 0.05 (0.61/0.78, minimum/maximum) and Jaccard's similarity coefficient of 0.55 ± 0.06 (0.44/0.64, minimum/maximum). For the caudate nucleus, the Hausdorff distance between manual and automatic segmented surface meshes was calculated with 3.40 ± 0.38 points (mean distance error: 1.94 ± 0.15 mm) (supplementary Figure A1 for representative individuals).

Tissue volumes (GM, WM, CSF) and brain indices ($I^{GM:WM}$, $I^{GM:brain}$, $I^{CSF:brain}$) of the underlying 16 subjects are given in Fig. 2C and in Table 2. The tissue volumes QCD were 0.158 (GM), 0.121 (WM), 0.271 (CSF), 0.187 ($I^{GM:WM}$), 0.073 ($I^{GM:brain}$) and 0.285 ($I^{CSF:brain}$).

Atlas labels

A total of 21 atlas labels were established. The labels included cerebral lobes, subcortical nuclei as well as WM tracts and cerebellar structures. Table 3 summarizes values and volumes off all labeled structures. In detail, the cerebrum was parcellated into temporal, parietal, occipital and frontal lobe (Fig. 4). The olfactory lobe equates with the NAV 2012 term *Pars basalis rhinencephali* and includes the following structures: olfactory bulb, peduncle, piriform lobe as well as the lateral olfactory and parahippocampal gyrus. Further, the cingulate gyrus, hippocampus, thalamus, lateral geniculate body and caudate nucleus were labeled separately (Fig. 5A and B). The cerebellar gray matter labels include hemispheres and the vermis (Fig. 5B). WM matter labels were created from the midsagittal corpus callosum, olfactory peduncle (without olfactory fascicles) and medullary body. Further, the internal CSF space was parcellated into the lateral ventricle, 4th ventricle, cerebral aqueduct, and the cranial part of the central canal (Fig. 5B).

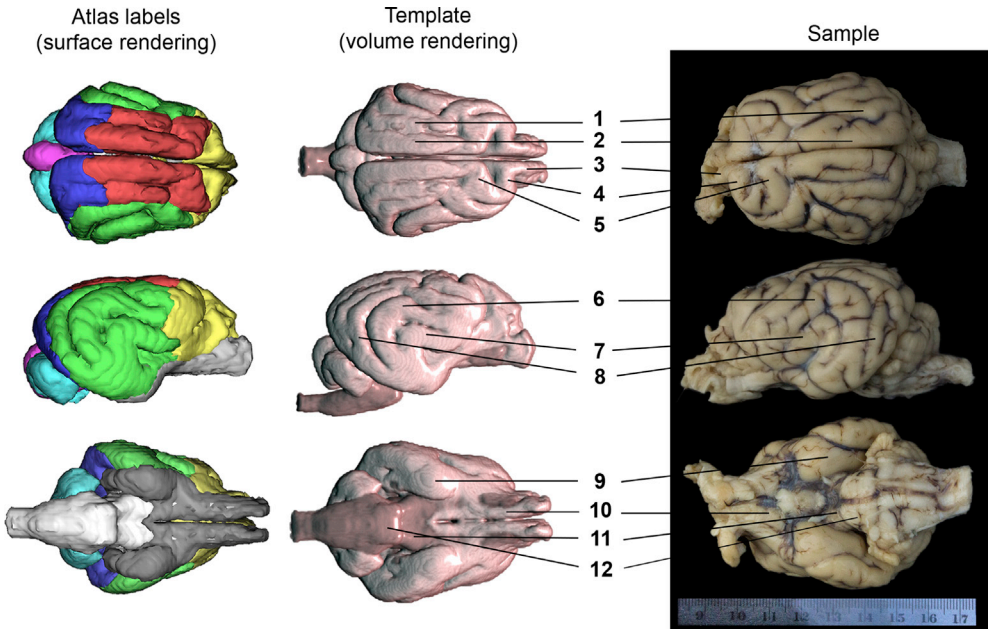

Fig. 4. Surface reconstruction of atlas labels, volume-rendered template and the brain sample. The surface rendering of the atlas labels are color-coded for better visualization: frontal (yellow), temporal (green), parietal (red) and occipital (blue) lobe, olfactory lobe (gray), cerebellar hemispheres (cyan), vermis (magenta). The brain tissue of the template was segmented and visualized as a 3D-rendered volume. 1 – Ectomarginal gyrus; 2 – Marginal gyrus; 3 – Prorean gyrus; 4 – Precruciate gyrus; 5 – Postcruciate gyrus; 6 – Ectosylvian gyrus; 7 – Sylvian gyrus; 8 – Ectomarginal gyrus; 9 – Caudal part of piriform lobe; 10 – Olfactory peduncle; 11 – Cerebral crus; 12 – Pons.

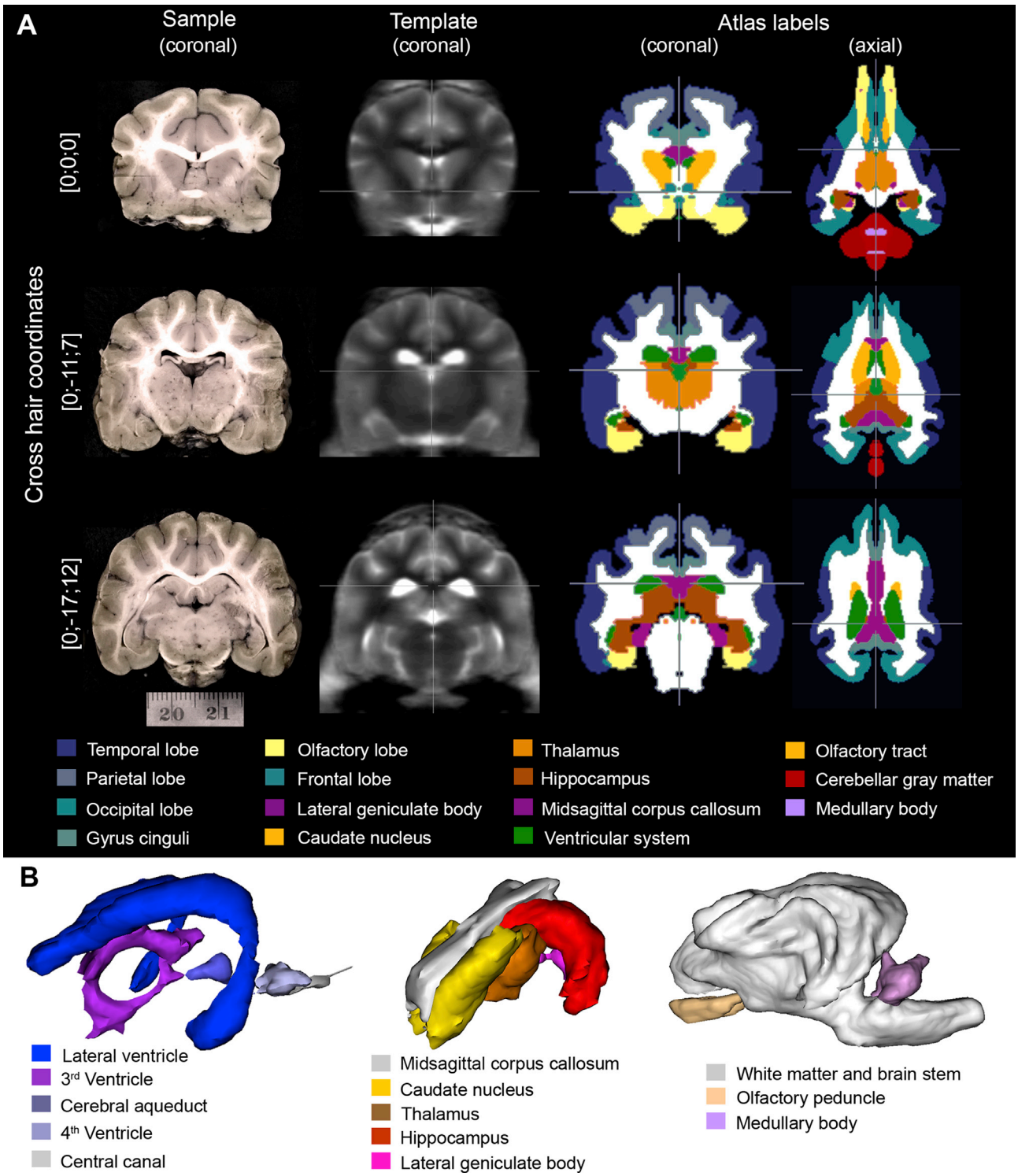

Fig. 5. Canine brain labels T2w template and brain slices. (A) Planes from a brain specimen (left, coronal plane), the T2w template (middle, coronal plane) and the canine brain atlas (right, croronal and axial plane), and retrieved from routine autopsy are aligned. Cross hair represents the coordinates in mm. A RGB lookup table was applied to the canine brain labels for better visualization. Labels of the ventriclular system and cerebellar gray matter were summarized. (B) 3D-surface rendering of the ventricular system labels (left), labels from subcortical structures (middle) and white matter (right).

Proof of principle for automated segmentation in SPM8

The automatic segmentation procedure resulted in sharply delineated GM, WM, and CSF tissue masks which matched well with the corresponding tissue in the respective T2w MRI data (see Fig. 6A). Nevertheless, detailed visual inspection of the segmented GM, WM, and CSF masks revealed one subject with obviously misclassified tissue classes. In particular, the subject (breed: Papillon, from Leipzig database) exhibited a dilated ventricle system (Fig. 6A) which resulted in a wrong classification of WM and CSF in favor to WM. Therefore, the subject was excluded from analysis. None of the other brain tissue masks showed any misclassification (see Fig. 6A).

Table 2
Description and demographics of the canine template and TPM.

Data format	NIFT-1, 32-bit float integer
Voxel size in mm ([x y z])	0.5 × 0.5 x 0.5 (110.5 × 120.5 x 228.5)
Stereotaxic origin [x y z] in mm (voxel)	55.5 × 60.5 x 53.5 (111 × 121 x 107)
Template tissue volumes in mL	GM: 34.08 WM: 21.20 CSF: 27.19
Canine breed and sex (male/female)	Labrador Retriever (1/2); Miniature Schnauzer (1/-); Hovawart (1/-); Hanoverian Scenthound (-/1); Border Collie (-/1); Shetland Sheepdog (-/1); Jack-Russel Terrier (-/1); Dalmatian (1/-); French Bulldog (1/-); Boxer (-/1); Beagle (1/-); Yorkshire Terrier (1/-); mixed breeds (2/-).
Tissue volumes in mL ± sd (I-III quartile)	GM: 36.1 ± 4.24 (32.7–41.3) WM: 23.1 ± 3.87 (22.7–25.37) CSF: 25.5 ± 7.71 (21.5–28.6)
Brain indices ±sd (I-III quartile):	$I^{GM:WM}$: 1.85 ± 0.361 (1.56–2.10) $I^{GM:brain}$: 0.64 ± 0.045 (0.61–0.68)

GM – gray matter; WM – white matter; CSF – cerebrospinal fluid.

Table 3
Characteristics of canine brain atlas labels.

Structure/NAV definition	Gray value[a]	Volume in mL
temporal lobe/*Lobus temporalis*	10	8.52
parietal lobe/*Lobus parietalis*	20	3.77
cingulate gyrus/*Gyrus cinguli*	40	1.65
occipital lobe/*Lobus occipitalis*	50	3.88
frontal lobe/*Lobus frontalis*	58	5.69
4th ventricle/*Ventriculus quartus*	80	0.09
cerebral aqueduct/*Aqueductus mesencephali*	90	0.03
3rd ventricle/*Ventriculus tertius*	100	0.22
lateral ventricle/*Ventriculus lateralis*	110	0.99
central canal/*Canalis centralis*	120	0.02
olfactory lobe/*Pars basalis rhinencephali*[b]	133	4.41
caudate nucleus/*Nucleus caudatus*	151	1.08
thalamus/*Thalamus*	161	1.29
hippocampus/*Hippocampus*[c]	171	1.36
cerebral hemisphere/*Hemispherium cerebelli*	181	2.12
vermis/*Vermis*	191	1.71
lateral geniculate body/*Corpus geniculatum laterale*	202	0.10
midsagittal corpus callosum/*Corpus callosum*	220	1.08
olfactory peduncle/*Pedunculus olfactorius*	230	0.29
medullary body/*Corpus medullare*	240	1.17

[a] - 8-bit range include rational positive integer values from 0 to 255 with 0 = background and 255 = non-labeled brain tissue.
[b] Including parahippocampal cortex.
[c] Including corpus geniculatum mediale; NAV – Nomina Anatomica Veterinaria.

The absolute GM, WM volume and brain indices ($I^{GM:WM}$, $I^{GM:brain}$) are given in Table 4. The data was not normally distributed (Kolmogorov Smirnov test, $p < 0.001$). The comparison between the Leipzig and Worcester datasets revealed a significant difference for WM volume ($p < 0.001$) while there was no statistical difference in GM volume ($p = 0.462$; Kruskal-Wallis-Test) (Fig. 6B). Consequently, the brain indices $I^{GM:WM}$ and $I^{GM:brain}$ were significantly lower in Leipzig dogs as compared to Worcester subjects ($p < 0.05$; Kruskal-Wallis-Test). As expected, the QCD for GM, WM and brain indices ($I^{GM:WM}$; $I^{GM:brain}$) of the Leipzig dataset were higher than the QCD for GM, WM and brain indices ($I^{GM:WM}$; $I^{GM:brain}$) of the Worcester dataset (see Table 4).

The canine atlas labels were successfully transformed into the appropriate individual space. The computed volume and QCD are summarized in Table 5. Overall, the homogeneous breed of the Worcester subjects showed a significantly decreased QCD of brain structures compared to the Leipzig dataset ($p < 0.001$, Kruskal-Wallis test). The QCD for hippocampus and frontal lobe from the Worcester dataset and the QCD of the midsagittal corpus callosum from the Leipzig dataset were higher than given by the 95% confidence interval (see Fig. 6C).

Discussion

We developed a breed-averaged, symmetric T2w TSE canine brain template and assigned the stereotaxic space according to the MNI definition. TPM for GM, WM and CSF are strictly aligned to the canine template and enable comparable as well as reproducible image post-processing. Moreover, we provide atlas labels aligned to the template and TPM to ensure a broad usability for anatomical discriminations or for atlas-based segmentation procedures.

In contrast to other approaches (Datta et al., 2012; Leigh et al., 2008) our tools include not only a population-averaged template with an increased number of subjects and breed, but also TPM, and a labeled brain atlas to be used with common software algorithms such as SPM or FSL. The reported template, together with the digital labeled atlas, enables coordinate allocation of distinct anatomical structures for different purposes involving the provided canine stereotaxic system (Mazziotta et al., 1995; Talairach and Tournoux, 1988) (Fox et al., 1985). By normalization to our canine reference system, these tools allow for objective and highly standardized targeting of anatomical structures. Additionally, the reported approach offers usability across different breeds without pre-allocating breed-specific considerations (see supplementary Figure A2). The co-registered GM, WM, and CSF TPM may serve as a starting point for highly precise, three-dimensional wrapping (e.g. using DARTEL, see supplementary Figure A3). They further enable morphological and volumetrical determination as well as voxel-wise analyses of individual canine brain structures (Klein et al., 2009; Zijdenbos et al., 1998) when used together with our binary-labeled canine atlas.

Quality of the data set

The resolution of MRI data generated with clinical scanners (as used in our study) is often lower than that provided by experimental high-field scanners. Moreover, MRI in animals requires general anesthesia which limits the scan duration and, consequently, resolution. To overcome this dilemma, we relied on adding a second plane for each subject (Leipzig2 dataset) involving the template and TPM to increase the information per voxel as well as contrast and detail resolution. While the resolution could not be increased simply by oversampling to 0.5 mm isotropic voxelsize, we aimed to minimize sampling errors on individual volumes by spatial non-local filtering and averaging multiple oversampled volumes (Fonov et al., 2011; Manjon et al., 2010). Thus, the template reconstruction was brought closer to the Nyquist limit. However, the observed decrease of CNR and SNR after normalization ($Avg2^{mean}$, see Fig. 2) indicates a relatively high inter-individual variation of local brain tissue compartments in different breeds (Leipzig dataset). This is also reflected in the relatively low standard deviation of local tissue compartments, what remains after applying a high-dimensional wrapping procedure ($Avg3^{mean}$, see Fig. 2, see supplementary Figure A4). Hence, the provided template is still somewhat blurry but preserved a relatively high number of details by the non-linear transformation algorithms. However, the template provides clearly discriminable and correctly demarcated brain tissue masks when our created TPM were used. These tissue masks are useful for further analysis and are highly suitable for e.g. voxel- or surface-based-morphometry. The phenotypic brain variation of all canine breeds may not be fully covered although a relatively high number of neurologically and radiologically inconspicuous subjects contributed to the T2w MRI template and TPM compared to other species (Munoz-Moreno et al., 2013; Saikali et al., 2010; Schweinhardt et al., 2003). This may deny particular breeds from being implemented in studies using automatic segmentation since misclassification errors may occur. The latter may also apply for neuropathological conditions significantly changing cerebral macroanatomy such as hydrocephalus (see results sections) (Schmidt et al., 2015).

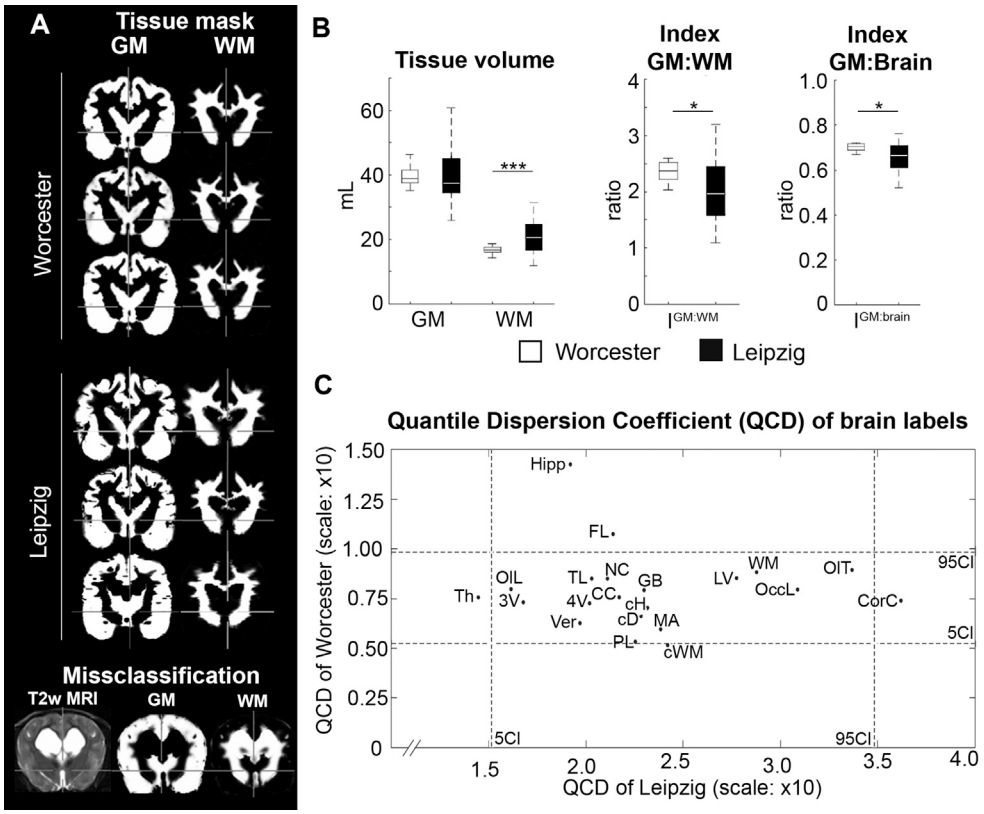

Fig. 6. Results of the proof-of-concept. (A) Representative tissue mask from Worcester (laboratory beagles) and Leipzig1 dataset (Hovawart, Dalmatian, Minature Schnauzer; from top to bottom) were shown. The only pseudo-misclassified MR data (breed: Papillon) is shown at bottom row. (B) Comparison of gray (GM), white matter (WM) volume and brain indices ($I^{GM:WM}$ and $I^{GM:Brain}$) between Leipzig and Worcester dataset. *p value < 0.05; **p-value < 0.01; ***p-value < 0.001 (Kruskal-Wallis test). (C) Comparative illustration of Quantile Coefficient of Dispersion (QCD) for label volumes of the Worcester and Leipzig dataset. Gray dotted line indicates the confidence interval (CI). 5CI – 5% confidence interval; 95CI – 95% confidence interval; Th – Thalamus; Hipp – Hippocampus; OlL – Olfactory lobe; 3V – 3rd ventricle; FL – Frontal lobe; TL – Temporal lobe; 4V – 4th ventricle; Ver – Vermis; NC – Caudate nucleus; CC - Gyrus cinguli; PL – Parietal lobe; cD – Central canal; GB – Lateral geniculate body; cH – Cerebellar hemisphere; MA – Cerebral aqueduct; cWM – Medullary body; LV – Lateral ventricle; WM – White matter; OccL – Occipital lobe; OlT – Olfactory peduncle; CorC – Midsagittal corpus callosum.

Table 4
Descriptive statistics of GM, WM, $I^{GM:WM}$ and $I^{GM:brain}$.

	Leipzig mean ± sd/QCD	Worcester mean ± sd/QCD
GM in mL	40.51 ± 9.12/0.267	39.49 ± 3.07/0.098
WM in mL	21.20 ± 5.45/0.369 ***	16.71 ± 1.17/0.094
$I^{GM:WM}$	2.01 ± 0.57/0.422 *	2.37 ± 0.17/0.129
$I^{GM:Brain}$	0.66 ± 0.07/0.142 *	0.70 ± 0.02/0.038

GM – gray matter; WM – white matter; CSF – cerebrospinal fluid. Significance level of Kruskal-wallis test: *p < 0.05, **p < 0.01; ***p < 0.001.

Table 5
Volumes (in mL) and quartile dispersion coefficients of canine brain structures for the Leipzig and Worcester datasets.

Label	Leipzig: Volume in mL ± sd/QCD	Worcester: Volume in mL ± sd/QCD
temporal lobe	8.99 ± 1.69/0.203	7.52 ± 0.50/0.085
parietal lobe	3.71 ± 0.67/0.225	2.92 ± 0.13/0.053
cingulate gyrus	1.77 ± 0.33/0.217	1.49 ± 0.10/0.076
occipital lobe	4.07 ± 0.97/0.309	2.94 ± 0.20/0.079
frontal lobe	5.11 ± 0.94/0.214	3.89 ± 0.29/0.107
4th ventricle	0.21 ± 0.04/0.202	0.17 ± 0.01/0.073
cerebral aqueduct	0.17 ± 0.03/0.238	0.14 ± 0.01/0.059
3rd ventricle	0.29 ± 0.08/0.168	0.21 ± 0.01/0.073
lateral ventricle	1.01 ± 0.55/0.277	0.59 ± 0.09/0.085
central canal	0.20 ± 0.04/0.228	0.17 ± 0.01/0.066
olfactory lobe	3.86 ± 0.57/0.161	3.18 ± 0.17/0.080
caudate nucleus	1.17 ± 0.19/0.211	1.04 ± 0.06/0.085
thalamus	1.32 ± 0.19/0.145	1.18 ± 0.09/0.075
hippocampus	1.39 ± 0.20/0.192	1.00 ± 0.15/0.143
cerebral hemisphere	2.19 ± 0.41/0.231	1.63 ± 0.08/0.070
vermis	1.80 ± 0.33/0.197	1.38 ± 0.07/0.063
lateral geniculate body	0.23 ± 0.04/0.230	0.20 ± 0.01/0.079
midsagittal corpus callosum	0.74 ± 0.18/0.362	0.71 ± 0.05/0.074
olfactory peduncle	0.34 ± 0.08/0.337	0.28 ± 0.08/0.089
medullary body	1.15 ± 0.29/0.242	1.11 ± 0.06/0.052

Automatic segmentation procedure using SPM

Despite potential limitations, our automatic segmentation procedure led to sharply demarcated, homogenous cerebral tissue masks facilitating further analysis. The TPM and template were derived by a symmetric approach adding a flipped copy of the dataset. Hence, an enhanced generalizability of the tissue classification may be assumed. This assumption is supported by the correct automatic segmentation of tissue classes of several additional breeds during the proof-of-concept study (see Table 2). So far, automatic image-processing of the canine brain was enabled only by using atlas-based segmentation procedures (Milne et al., 2016). Unfortunately, that approach necessitates high-dimensional warping procedures of the reference template, which comes along with decreased robustness and requires high computational power (Kazemi and Noorizadeh, 2014). These approaches also (i) lack a proof at a wider population range including different breeds and (ii) do not take into account that the assumed classification criteria 'scull phenotype' may be dominated by the facial bones, and not by the brain cavity (Packer et al., 2015). Importantly, earlier reports about automatic segmentation without TPMs were shown to be erroneous for canine brains (Kazemi and Noorizadeh, 2014; Tapp et al., 2006). Here, we demonstrate an unbiased, robust and reproducible method and related processing tools for automatic brain tissue segmentation of different breeds with freely available software packages.

Atlas labels

Twenty-one atlas labels were defined according to established nomenclature standards (Adrianov et al., 2010), and were named according to NAV 2012 (Constantinescu et al., 2012). Every label was manually delineated by observing all three T2w MRI template planes. However, the atlas labels were based on visual representation of the breed-averaged T2w MRI template and, thus, represent an enhanced generalizability as compared to previously reported individual atlases

(Leigh et al., 2008). Further refinement is required for a more detailed parcellation of brain structures, for instance by aligning digitized histological specimens to the MRI template as established for other species (Bai et al., 2012; Newman et al., 2009; Nie et al., 2013). The atlas labels allow for automatic identification and volumetric/morphometric analysis by common software packages and, thus, were implemented for the subsequent proof of concept study.

Comparison of a heterogeneous clinical cohort with a homogenous beagle population

Overall, the total brain volume of dogs was determined to be about 61 mL, which is in contrast to descriptions in literature (77 mL) (Schmidt et al., 2014). This discrepancy may indicate a variation of brain tissue volume in different breeds because giant breeds were included into the aforementioned study, but may also illustrate artifacts from retrospective comparison without appropriate reference parameters (such as total WM or threshold values). Hence, the disadvantages of a manual or even semi-automatic segmentation procedures (in particular subjectivity, labor-intensity, and limited reproducibility) became obvious (Zijdenbos et al., 1998). However, the presented approach served as a proof-of-concept for the usability of automatic segmentation procedures since we are aware that the given cohort may not fully represent all canine phenotypes. Hence, we did not consider potential other influences on brain volumetry, such as individual body size and weight.

The homogenous cohort of the laboratory beagles from the Worcester dataset showed a slightly decreased WM volume as compared to the clinical cohort of the Leipzig dataset. This became also caused significantly increased $I^{GM:WM}$ and $I^{GM:brain}$ indices. The reason for this cannot be clearly defined, but the high degree of inbreeding in laboratory beagles should be considered as a potential reason for this variation. Moreover, slight differences in MRI sequences (see Table 1) may have had an effect as well, because the data was retrieved from previous studies and not solely generated for our study.

The $I^{GM:Brain}$ index in dogs (0.64, see Table 2) is slightly higher as compared to humans (0.55) (Luders et al., 2002), non-human primates (0.58) (Chen et al., 2013) and sheep (0.59) (Nitzsche et al., 2015). A potential explanation is that the canine segmentation procedure also included cerebellar tissue components.

Importantly, the dispersion of the GM and WM volume as well as brain indices given by QCD are 3-fold higher in the Leipzig dataset as compared to the Worcester one. Detailed analysis of individual atlas labels revealed high QCD for the frontal lobe and the hippocampus formation in the homogenous Worcester cohort. Both structures play an important role in cognition and, thus, the differences between the environment keeping laboratory beagles and pet dogs, should be taken into account. However, this supports the demand for considering the breed in particular during scientific research targeting cognition and/or motor system (Cook et al., 2016). Further studies are required to identify the neurological and/or behavioral consequence of volumetrical variation of both structures in clinically relevant breeds (Schmidt et al., 2015).

Interestingly, the QCD of the midsagittal corpus callosum exceeded the 95% CI in the heterogeneous Leipzig group while in this group the QCD of frontal lobe and hippocampus were moderate. This finding may reflect the interbreed variability and different social and environmental interaction, and therefore, a varying stimulation of the corpus callosum should also to be taken into account. This support the demand for considering the breed in particular during scientific research targeting cognition and/or motoric system (Cook et al., 2016).

Perspective

The breed-specific variation of canine brain anatomy is illustrated by the detected local standard deviation during template processing. Unfortunately, information about the influence of the phenotype manipulation by selective breeding on brain anatomy is lacking, especially for extreme breeds such as brachycephalic dogs. Consequently, establishing a reference for *Canis lupus familiaris* may become difficult when trying to systematically determine phenotypical factors. Further studies will (i) strongly demand a larger cohort and, subsequently, knowledge of its morphological variation, and (ii) refine the established tools for further reproducible and objective detail analysis. The work presented herein will be the foundation for such a study and, subsequently, characterization and classification of different brain phenotypes. The approach suggested herewith is free of assumptions regarding non-cerebral tissue and therefore may provide a more objective basis for further detailed atlas creation. The data can serve as a starting point to clarify the association between breed-specific phenotype and brain morphology. Further analyses may consider (i) the number of subjects, (ii) reliability of MRI techniques, (iii) neuopathological-cognitive aspects, (iv) phenotypical characteristics of the breed and, (v) the reproducibility of the analysis techniques.

Conclusion

The presented data set including a breed-averaged symmetric T2w TSE canine brain template, TPM and a labeled canine brain atlas enables a detailed processing of structural brain images for tissue classification and spatial analysis for several canine breeds. The cerebral morphology highly varies between different breeds when compared to a homogenous beagle group. Further systematic analyses are required to determine the effect of selective breeding on cerebral phenotypic variation.

Public data availability

All image data were stored in NIFTI-1 format and include a resolution of 0.5 mm isothropic voxel size. The data can be viewed in most common imaging software including SPM, FSL (Analysis Group, FMRIB, Oxford, UK) (Smith et al., 2004) and other packages. The T2w TSE template, TPM, atlas labels and a T2w sample image are freely available at http://animal-brain-mapping.com.

Conflict of interest statement

No conflict to be reported.

Acknowledgment

The authors thank Prof. Dr. med. Osama Sabri, Department for Nuclear Medicine, University Hospital of Leipzig, Leipzig, Germany for supporting the project and Ralf-Peter Dobroschke from the Institute of Veterinary Pathology, University Leipzig for the preparation of the canine brain.

Appendix A. Supplementary data

Supplementary data related to this article can be found at https://doi.org/10.1016/j.neuroimage.2018.01.066.

References

Adrianov, O., Domino, K., Domino, E., 2010. Atlas of the Canine Brain. Npp Books.
Ashburner, J., 2007. A fast diffeomorphic image registration algorithm. Neuroimage 38 (1), 95–113. https://doi.org/10.1016/j.neuroimage.2007.07.007.
Ashburner, J., Friston, K.J., 2000. Voxel-based morphometry–the methods. Neuroimage 11 (6 Pt 1), 805–821. https://doi.org/10.1006/nimg.2000.0582.
Ashburner, J., Friston, K.J., 2005. Unified segmentation. Neuroimage 26 (3), 839–851. https://doi.org/10.1016/j.neuroimage.2005.02.018.
Ashburner, J., Friston, K., 2011. Computational anatomy. In: Penny, W.D., Friston, K.J., Ashburner, J.T., Kiebel, S.J., Nichols, T.E. (Eds.), Statistical Parametric Mapping: The Analysis of Functional Brain Images. Elsevier Science, pp. 49–98.
Bai, J., Trinh, T.L., Chuang, K.H., Qiu, A., 2012. Atlas-based automatic mouse brain image segmentation revisited: model complexity vs. image registration. Magn. Reson. Imaging 30 (6), 789–798 doi: S0730-725X(12)00051-3 [pii];10.1016/j.mri.2012.02.010 [doi].

Beauchemin, M., Thomson, K., Edwards, G., 1998. On the Hausdorff distance used for the evaluation of segmentation results. Can. J. Rem. Sens. 24 (1), 3–8.

Bernardino, F., Rentmeister, K., Schmidt, M.J., Bruehschwein, A., Matiasek, K., Matiasek, L.A., et al., 2015. Inferior cerebellar hypoplasia resembling a Dandy-Walker-like malformation in purebred Eurasier dogs with familial non-progressive ataxia: a retrospective and prospective clinical cohort study. PLoS One 10 (2), e0117670. https://doi.org/10.1371/journal.pone.0117670.

Chen, X., Errangi, B., Li, L., Glasser, M.F., Westlye, L.T., Fjell, A.M., et al., 2013. Brain aging in humans, chimpanzees (Pan troglodytes), and rhesus macaques (Macaca mulatta): magnetic resonance imaging studies of macro- and microstructural changes. Neurobiol. Aging 34 (10), 2248–2260. https://doi.org/10.1016/j.neurobiolaging.2013.03.028.

Constantinescu, G.M., Gheorghe, M., Schaller, O., 2012. Illustrated Veterinary Anatomical Nomenclature, 3 ed. Enke, Stuttgart.

Cook, P.F., Spivak, M., Berns, G., 2016. Neurobehavioral evidence for individual differences in canine cognitive control: an awake fMRI study. Anim Cogn. https://doi.org/10.1007/s10071-016-0983-4.

Datta, R., Lee, J., Duda, J., Avants, B.B., Vite, C.H., Tseng, B., et al., 2012. A digital atlas of the dog brain. PLoS One 7 (12), e52140. https://doi.org/10.1371/journal.pone.0052140.

Dilks, D.D., Cook, P., Weiller, S.K., Berns, H.P., Spivak, M., Berns, G.S., 2015. Awake fMRI reveals a specialized region in dog temporal cortex for face processing. PeerJ 3, e1115. https://doi.org/10.7717/peerj.1115, 1115 [pii].

Fonov, V., Evans, A.C., Botteron, K., Almli, C.R., McKinstry, R.C., Collins, D.L., 2011. Unbiased average age-appropriate atlases for pediatric studies. Neuroimage 54 (1), 313–327. https://doi.org/10.1016/j.neuroimage.2010.07.033.

Fox, P.T., Perlmutter, J.S., Raichle, M.E., 1985. A stereotactic method of anatomical localization for positron emission tomography. J. Comput. Assist. Tomogr. 9 (1), 141–153.

Frey, S., Pandya, D.N., Chakravarty, M.M., Bailey, L., Petrides, M., Collins, D.L., 2011. An MRI based average macaque monkey stereotaxic atlas and space (MNI monkey space). Neuroimage 55 (4), 1435–1442. https://doi.org/10.1016/j.neuroimage.2011.01.040.

Gaser, C., Dahnke, R., 2016. CAT-A computational anatomy Toolbox for the analysis of structural MRI data. HBM 336–348.

Kazemi, K., Noorizadeh, N., 2014. Quantitative comparison of SPM, FSL, and brainsuite for brain MR image segmentation. J Biomed Phys Eng. 4 (1), 13–26.

Klein, A., Andersson, J., Ardekani, B.A., Ashburner, J., Avants, B., Chiang, M.C., et al., 2009. Evaluation of 14 nonlinear deformation algorithms applied to human brain MRI registration. Neuroimage 46 (3), 786–802. https://doi.org/10.1016/j.neuroimage.2008.12.037.

Leigh, E.J., Mackillop, E., Robertson, I.D., Hudson, L.C., 2008. Clinical anatomy of the canine brain using magnetic resonance imaging. Vet. Radiol. Ultrasound 49 (2), 113–121.

Li, X., Morgan, P.S., Ashburner, J., Smith, J., Rorden, C., 2016. The first step for neuroimaging data analysis: DICOM to NIfTI conversion. J. Neurosci. Meth. 264, 47–56. https://doi.org/10.1016/j.jneumeth.2016.03.001.

Luders, E., Steinmetz, H., Jancke, L., 2002. Brain size and grey matter volume in the healthy human brain. Neuroreport 13 (17), 2371–2374. https://doi.org/10.1097/01.wnr.0000049603.85580.da.

Manjon, J.V., Coupe, P., Marti-Bonmati, L., Collins, D.L., Robles, M., 2010. Adaptive non-local means denoising of MR images with spatially varying noise levels. J. Magn. Reson. Imag. 31 (1), 192–203. https://doi.org/10.1002/jmri.22003.

Mazziotta, J.C., Toga, A.W., Evans, A., Fox, P., Lancaster, J., 1995. A probabilistic atlas of the human brain: theory and rationale for its development. The International Consortium for Brain Mapping (ICBM). Neuroimage 2 (2), 89–101 doi: S1053811985710129.

Milne, M.E., Steward, C., Firestone, S.M., Long, S.N., O'Brien, T.J., Moffat, B.A., 2016. Development of representative magnetic resonance imaging-based atlases of the canine brain and evaluation of three methods for atlas-based segmentation. Am. J. Vet. Res. 77 (4), 395–403. https://doi.org/10.2460/ajvr.77.4.395.

Munoz-Moreno, E., Arbat-Plana, A., Batalle, D., Soria, G., Illa, M., Prats-Galino, A., et al., 2013. A magnetic resonance image based atlas of the rabbit brain for automatic parcellation. PLoS One 8 (7), e67418. https://doi.org/10.1371/journal.pone.0067418.

Newman, J.D., Kenkel, W.M., Aronoff, E.C., Bock, N.A., Zametkin, M.R., Silva, A.C., 2009. A combined histological and MRI brain atlas of the common marmoset monkey, Callithrix jacchus. Brain Res. Rev. 62 (1), 1–18. https://doi.org/10.1016/j.brainresrev.2009.09.001.

Nie, B., Chen, K., Zhao, S., Liu, J., Gu, X., Yao, Q., et al., 2013. A rat brain MRI template with digital stereotaxic atlas of fine anatomical delineations in paxinos space and its automated application in voxel-wise analysis. Hum. Brain Mapp. 34 (6), 1306–1318. https://doi.org/10.1002/hbm.21511.

Nitzsche, B., Frey, S., Collins, L., Seeger, J., Lobsien, D., Dreyer, A., et al., 2015. A stereotaxic, population-averaged T1w ovine brain atlas including cerebral morphology and tissue volumes. Front. Neuroanat. 9 https://doi.org/10.3389/fnana.2015.00069.

Noh, D., Choi, S., Choi, H., Lee, Y., Lee, K., 2017. Evaluation of interthalamic adhesion size as an indicator of brain atrophy in dogs with and without cognitive dysfunction. Vet. Radiol. Ultrasound. https://doi.org/10.1111/vru.12528.

Packer, R.M., Hendricks, A., Tivers, M.S., Burn, C.C., 2015. Impact of facial conformation on canine health: brachycephalic obstructive airway syndrome. PLoS One 10 (10), e0137496. https://doi.org/10.1371/journal.pone.0137496.

Papp, E.A., Leergaard, T.B., Calabrese, E., Johnson, G.A., Bjaalie, J.G., 2014. Waxholm space atlas of the sprague dawley rat brain. Neuroimage 97, 374–386. https://doi.org/10.1016/j.neuroimage.2014.04.001.

Saikali, S., Meurice, P., Sauleau, P., Eliat, P.A., Bellaud, P., Randuineau, G., et al., 2010. A three-dimensional digital segmented and deformable brain atlas of the domestic pig. J. Neurosci. Meth. 192 (1), 102–109. https://doi.org/10.1016/j.jneumeth.2010.07.041.

Schindelin, J., Arganda-Carreras, I., Frise, E., Kaynig, V., Longair, M., Pietzsch, T., et al., 2012. Fiji: an open-source platform for biological-image analysis. Nat Methods. 9 (7), 676–682. https://doi.org/10.1038/nmeth.2019.

Schmidt, M.J., Amort, K.H., Failing, K., Klingler, M., Kramer, M., Ondreka, N., 2014. Comparison of the endocranial- and brain volumes in brachycephalic dogs, mesaticephalic dogs and Cavalier King Charles spaniels in relation to their body weight. Acta Vet. Scand. 56, 30. https://doi.org/10.1186/1751-0147-56-30.

Schmidt, M.J., Laubner, S., Kolecka, M., Failing, K., Moritz, A., Kramer, M., et al., 2015. Comparison of the relationship between cerebral white matter and grey matter in normal dogs and dogs with lateral ventricular enlargement. PLoS One 10 (5), e0124174. https://doi.org/10.1371/journal.pone.0124174.

Schweinhardt, P., Fransson, P., Olson, L., Spenger, C., Andersson, J.L., 2003. A template for spatial normalisation of MR images of the rat brain. J. Neurosci. Meth. 129 (2), 105–113 doi: S0165027003001924.

Sled, J.G., Zijdenbos, A.P., Evans, A.C., 1998. A nonparametric method for automatic correction of intensity nonuniformity in MRI data. IEEE Trans. Med. Imag. 17 (1), 87–97. https://doi.org/10.1109/42.668698.

Smith, S.M., Jenkinson, M., Woolrich, M.W., Beckmann, C.F., Behrens, T.E., Johansen-Berg, H., et al., 2004. Advances in functional and structural MR image analysis and implementation as FSL. Neuroimage 23 (Suppl. 1), S208–S219. https://doi.org/10.1016/j.neuroimage.2004.07.051.

Su, M.Y., Tapp, P.D., Vu, L., Chen, Y.F., Chu, Y., Muggenburg, B., et al., 2005. A longitudinal study of brain morphometrics using serial magnetic resonance imaging analysis in a canine model of aging. Prog. Neuro-Psychopharmacol. Biol. Psychiatry 29 (3), 389–397. https://doi.org/10.1016/j.pnpbp.2004.12.005.

Talairach, J., Tournoux, P., 1988. Co-planar Stereotaxic Atlas of the Human Brain: 3-dimensional Proportional System. Thieme Medical Pub.

Tapp, P.D., Head, K., Head, E., Milgram, N.W., Muggenburg, B.A., Su, M.Y., 2006. Application of an automated voxel-based morphometry technique to assess regional gray and white matter brain atrophy in a canine model of aging. Neuroimage 29 (1), 234–244. https://doi.org/10.1016/j.neuroimage.2005.07.043.

Xiao, Y., Fonov, V., Chakravarty, M.M., Beriault, S., Al, S.F., Sadikot, A., et al., 2017. A dataset of multi-contrast population-averaged brain MRI atlases of a Parkinsons disease cohort. Data Brief. 12, 370–379. https://doi.org/10.1016/j.dib.2017.04.013.

Zijdenbos, A., Forghani, R., Evans, A., 1998. Automatic quantification of MS lesions in 3D MRI brain data sets: validation of INSECT. In: Wells, W., Colchester, A., Delp, S. (Eds.), Medical Image Computing and Computer-assisted Interventation - MICCAI 1998, 1496 ed. Springer Berlin Heidelberg, pp. 439–448.